3

Digital Hologram Processing in On-Axis Holography

Corinne Fournier, Loïc Denis, Mozhdeh Seifi and Thierry Fournel
Laboratoire Hubert Curien, Saint Etienne University, France

3.1 Introduction

The quantitative three-dimensional reconstruction and tracking of micro or nano objects spread in a volume is of great interest in many fields of science, such as in biomedical fields (e.g., tracking of markers), fluid mechanics (e.g., the study of turbulence or evaporation phenomena), and chemical engineering (e.g., the study of reactive multiphase flow), among many other applications. The development of accurate and high-speed 3-D imaging systems is crucial in these fields. Several imaging techniques have been investigated during the last 20 years, such as 3-D Particle Tracking Velocimetry with four cameras (Virant and Dracos 1997) or extended Laser Doppler Anemometry (Volk *et al*. 2008). Three-dimensional tracking has been performed with single-molecule fluorescent microscopy using nanometer-sized fluorescent markers based on astigmatism optics (Huang *et al*. 2008), double-helix PSF (Pavani *et al*. 2009), or multi-plane detection (Pavani *et al*. 2009). Each of these techniques has its own advantages and limitations but none of these techniques can yet compete in accuracy with digital holography (DH) to reconstruct 3-D trajectories and size of high speed moving objects.

DH is a non invasive 3-D metrological tool that is suitable for fast moving object reconstruction and sizing. It has proved to be efficient in many fields. Some recent examples include: Verpillat *et al*. (2011); Chareyron *et al*. (2012); El Mallahi *et al*. (2013); Lamadie *et al*. (2012); Moon *et al*. (2013) and Seifi *et al*. (2013b).

Two setups are commonly used in DH: the on-axis setup and the off-axis setup. Although off-axis setups are well adapted to the reconstruction of object surface, the on-axis setups are more suited to accurate reconstruction of micro or nano objects in a volume. In contrast to off-axis holography, on-axis hologram exploits the whole frequency bandwidth of the sensor to encode the depth of objects with high accuracy. Furthermore because it does not involve

Multi-dimensional Imaging, First Edition. Edited by Bahram Javidi, Enrique Tajahuerce and Pedro Andrés.

beam splitters, mirrors, and lenses, the in-line setup (i.e., Gabor setup) is less sensitive to vibrations. This imaging technique is also called "lensless imaging" (Faulkner and Rodenburg 2004; Repetto *et al*. 2004; Allier *et al*. 2010; Fienup 2010), because it involves no lens between the object and the sensor. The disadvantage of on-axis setups comes from the superimposition of a background to the hologram signal, thereby reducing the dynamic range of the signal of interest.

Over the past decade, numerous algorithms for the analysis of digital holograms have been proposed (several journal special issues were published on the subject: see Poon *et al*. 2006; Coupland and Lobera 2008, Kim *et al*. 2013). These reconstruction algorithms are mostly based on a common approach (hereafter denoted the classical approach): a digital reconstruction based on the simulation of hologram diffraction.

In contrast to this optical approach, signal processing tools commonly used in the image processing of other imaging modalities provide a rigorous way to process on-axis holograms leading to optimal image processing in certain cases. Rather than transforming the hologram, the aim is to find the reconstruction that best models the measured hologram. This "inverse problems" approach extracts more information from the hologram and is proved to solve two essential problems in digital holography: the improvement of accuracy of reconstruction and enlargement of the studied field beyond the physical limit of the sensor size (Soulez *et al*. 2007a,b). It also leads to almost unsupervised algorithms (only few tuning parameters are used). These approaches are sometimes referred to as *compressive sensing methods* (Brady *et al*. 2009, Lim *et al*. 2011, Rivenson *et al*. 2010). The drawback of these approaches is a computational load heavier than with classical techniques. The parameters that increase the processing time are the size of the reconstructed volume, the number of parameters to estimate (in the case of parametric reconstruction), and the model complexity. Accelerations have been recently proposed to reduce processing time.

The second section of the chapter defines the framework of hologram processing and introduces hologram-image formation models and the mathematical notations used in the following. In the third section, we briefly remind that, from a signal processing point of view, the light propagation operator classically used to reconstruct holograms does not invert hologram formation. Then, Section 3.4 gives a unified presentation of hologram processing methods based on inverse problems. We present in Section 3.5 an estimate of the parameter accuracy lower bound reachable using such algorithms. In Section 3.6, recent algorithms aimed at reducing the complexity of the reconstruction are presented.

3.2 Model of Hologram Image Formation

In this section, we remind the reader of the mathematical model of hologram formation (Goodman 1996) that will be used in the reconstruction methods described in the next sections. We also introduce the matrix notations, commonly used in inverse problem frameworks, allowing us to account easily for sampling and cropping of the signal for theoretical analysis of the problem. We consider an on-axis holography setup where n small objects are illuminated with a collimated laser beam. We assume that the Royer criterion is satisfied (i.e., that the surface of the projected objects on the sensor is less than 1% of the sensor area, see Royer

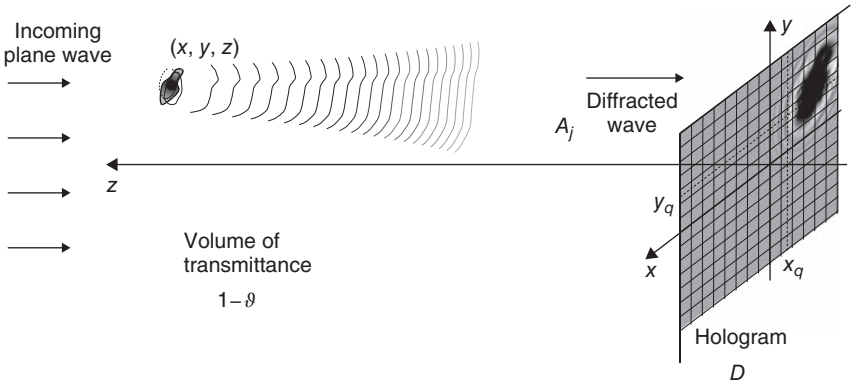

Figure 3.1 Illustration of in-line hologram formation model

1974). The digital camera records both the object wave–the wave that has propagated from the objects to the sensor–and the reference wave–the illuminating wave–(see Fig. 3.1). This diffraction phenomenon can also be modeled as interferences between the waves diffracted by each object aperture ϑ_j and the illuminating wave A_{ref} (assumed to be unaltered by the diffracting objects).

We consider small objects and that Fresnel's diffraction approximation is valid (Goodman 1996, p. 69), that is, for a propagating distance z, a width of object l and a wavelength λ the following condition is satisfied: $z^3 \gg \pi\ l^4/(64\lambda)$. For most experimental conditions Fresnel's approximation is valid (e.g., for a laser wavelength $\lambda = 532$ nm, and an object width $l \approx 100$ µm the minimum distance to the detector $z_{min} = 0.5$ mm). Under such conditions and for n particles of radii r_j and 3-D positions (x_j, y_j, z_j), the intensity measured by the detector at position (x, y) is given by (Seifi *et al.* 2013b):

$$\mathrm{I}(x,y) = I^0_{ref}(x,y) - 2\sqrt{I^0_{ref}(x,y)} \sum_{j=1}^{n} \eta_j . \Re[(h_{z_j} * \vartheta_j)(x,y)] + \beta(x,y), \tag{3.1}$$

where I^0_{ref} stands for the intensity of the reference wave on the hologram plane (background image), the real factors η_j accounting for possible variations of incident energy seen by an object due to the non-uniformity of the reference wave, ϑ_j is the complex aperture of the j^{th} object, and h_{z_j} is the impulse response function for free space propagation over a distance z_j (distance of the j^{th} object to the hologram). β represents the sum of second-order terms of diffraction. Under Fresnel approximation, the impulse response is the so-called Fresnel function:

$$h_{z_j}(x,y) = \frac{1}{i\lambda z_j} \exp\ \left(\frac{i\pi(x^2+y^2)}{\lambda z_j} \right). \tag{3.2}$$

Let us note that other kernels can be used depending on the experimental conditions (e.g., Rayleigh–Sommerfeld kernel: Goodman 1996).

For small objects and large distances between objects and sensor (i.e., $\pi l^2/(4\lambda z) \ll 1$) the second order terms of Eq. (3.1) are negligible. The model then simplifies to a linear model:

$$I(x,y) = I^0_{ref}(x,y) + \sqrt{I^0_{ref}(x,y)} \sum_{j=1}^{n} \alpha_j . m_j(x,y),$$

$$\text{with} \quad m_j(x,y) = -\Re(h_{z_j} * \vartheta_j)(x,y),$$

$$\alpha_j = 2\,\eta_j. \tag{3.3}$$

The digitization of intensity I on an N-pixel camera leads to a digital hologram. To remove the terms in Eq. (3.3) that don't depend on the object patterns (e.g., the background I^0_{ref}), a background image is usually calculated either by taking an image of an empty volume, or recording a video of holograms and calculating the mean image of this video. To efficiently remove the effect of background, an element-wise subtraction of I^0_{ref} followed by an element-wise division of the result by $\sqrt{I^0_{ref}}$ is performed on the digital hologram. The digital image obtained D is therefore modeled as a sum of diffraction patterns:

$$D(x,y) = \sum_{j=1}^{n} \alpha_j . m_j(x,y). \tag{3.4}$$

The digital hologram can be expressed in a vector form $\boldsymbol{d}$ of N grayvalues. Depending on the application, it may be related to the diffraction pattern of each object (FI, see illustration Fig. 3.2), or to the opacity distribution of the objects (FII, see illustration Fig. 3.3):

$$\text{(FI)} \qquad \boldsymbol{d} = \boldsymbol{M}\,\boldsymbol{\alpha} + \boldsymbol{\epsilon} \qquad \leftrightarrow \qquad \begin{bmatrix} D(x_1,y_1) \\ \vdots \\ D(x_N,y_N) \end{bmatrix} = \begin{bmatrix} \sum_j \alpha_j m_j(x_1,y_1) + \epsilon_1 \\ \vdots \\ \sum_j \alpha_j m_j(x_N,y_N) + \epsilon_N \end{bmatrix} \tag{3.5}$$

$$\text{(FII)} \qquad \boldsymbol{d} = \boldsymbol{H}\,\boldsymbol{\vartheta} + \boldsymbol{\epsilon} \qquad \leftrightarrow \qquad \begin{bmatrix} D(x_1,y_1) \\ \vdots \\ D(x_N,y_N) \end{bmatrix} = \begin{bmatrix} \sum_k \left[h_{z_k} * \vartheta_k\right](x_1,y_1) + \epsilon_1 \\ \vdots \\ \sum_k [h_{z_k} * \vartheta_k](x_N,y_N) + \epsilon_N \end{bmatrix} \tag{3.6}$$

Equations (3.5) and (3.6) are written in compact form using matrix notation. In words, Eq. (3.5) expresses the recorded hologram $\boldsymbol{d}$ as the sum of the diffraction patterns of each object ($\boldsymbol{M}\,\boldsymbol{\alpha}$), a perturbation term accounting for the different sources of noise and for our modeling approximations ($\boldsymbol{\epsilon}$). The term $\boldsymbol{M}\,\boldsymbol{\alpha}$ is the product between a $N \times n$ matrix ($\boldsymbol{M}$) and a n elements vector ($\boldsymbol{\alpha}$). Matrix $\boldsymbol{M}$ may be thought of as a dictionary of the diffraction patterns of n objects (the j-th column of matrix $\boldsymbol{M}$ corresponds to the N graylevels of the diffraction pattern of the j-th object: $[m_j(x_1,y_1), \cdots, m_j(x_N,y_N)]^t$). Vector $\boldsymbol{\alpha}$ defines the amplitude of each of the n diffraction patterns. Equation (3.5) thus corresponds to a discretization of Eq. (3.3).

Equation (3.6) expresses the hologram $\boldsymbol{d}$ as the sum of diffraction patterns $\boldsymbol{H}\,\boldsymbol{\vartheta}$ created by the opacity distribution $\boldsymbol{\vartheta}$ and a noise term ($\boldsymbol{\epsilon}$). If the opacity distribution is defined over K planes of L pixels, $\boldsymbol{\vartheta}$ is a vector of $K \cdot L$ elements corresponding to the stacking of all opacity values.

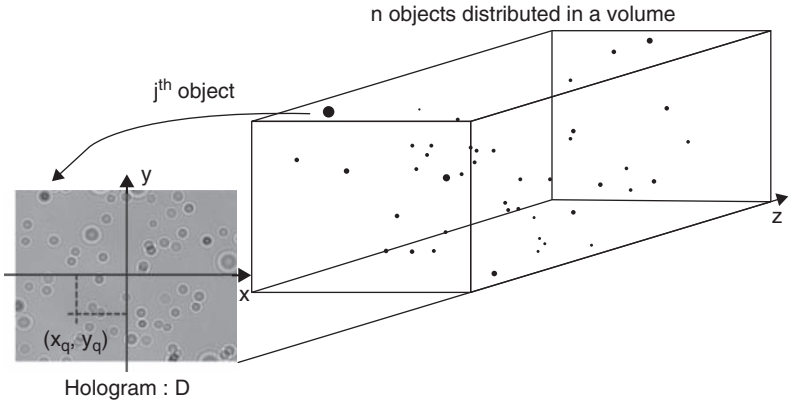

Figure 3.2 Illustration of parametrical objects image-hologram formation (FI)

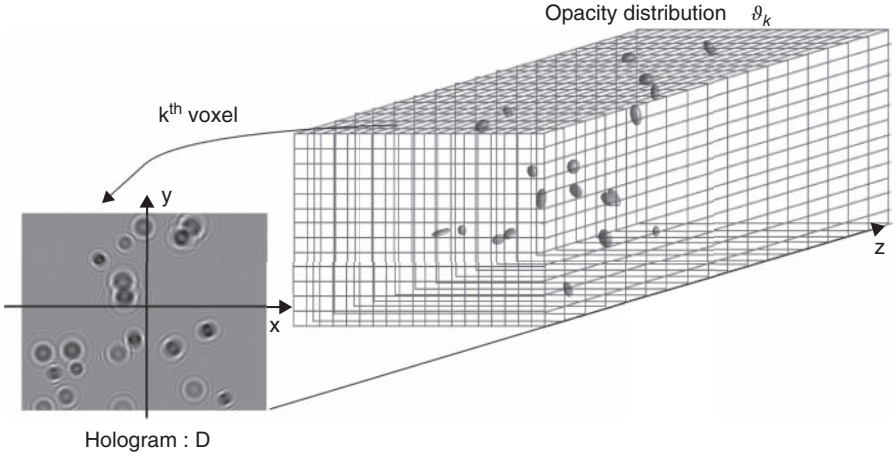

Figure 3.3 Illustration of the image-hologram formation computed from opacity distribution of the studied volume (FII)

$\boldsymbol{H}$ is then a $N^2 \times K \cdot L^2$ matrix corresponding to a (discrete) diffraction operator. Each column of $\boldsymbol{H}$ is a discretization of the impulse response kernel h, that is, the diffraction pattern on the hologram created by a point-like opaque object at a given 3-D location. $\boldsymbol{H}\ \boldsymbol{\vartheta}$ corresponds to the summation of the convolution of the opacity distribution in each plane z by the impulse response kernel of distance z.

Matrices $\boldsymbol{M}$ and $\boldsymbol{H}$ are written formally to clarify the proposed models and the derived reconstruction in the subsequent sections. It is worth noting that, in practice, they are neither stored nor explicitly multiplied to vectors $\boldsymbol{\alpha}$ and $\boldsymbol{\vartheta}$. Due to (transversal) shift-invariance of models m_j and kernels h_j, the products $\boldsymbol{M}\ \boldsymbol{\alpha}$ and $\boldsymbol{H}\ \boldsymbol{\vartheta}$ can be computed using fast Fourier transforms (Denis *et al*. 2009b, Soulez *et al*. 2007b).

Pixel integration on the camera can be taken into account in matrices $\boldsymbol{M}$ and $\boldsymbol{H}$ by convolving the diffraction patterns m_j and diffraction kernels h_{z_k} (which form the matrix columns) with a 2-D rectangular function with the same area as the pixel's sensitive area.

3.3 DH Reconstruction Based on Back Propagation

Most of the methods for reconstructing digital holograms are based on the simulation of an optical reconstruction, followed by analysis of the 3-D reconstructed volume. In all-optical holography, after a hologram has been recorded and the holographic plate has been processed, the plate is re-illuminated with the reference wave. Hologram diffraction creates a virtual (i.e., defocused) and a real (i.e., focused) image. In digital holography, the holographic plate is replaced by a digital camera whose sensor size and resolution is worse by several orders of magnitude. The simulation of hologram diffraction, though straightforward to implement (and fast), leads to sub-optimal reconstructions with distortions due to boundary effects and the presence of the virtual (twin) image. In this section, we present hologram-diffraction based approaches and their limitations.

The classical 3-D reconstruction of digital holograms is performed in two steps. The first step is based on a numerical simulation of the optical reconstruction. A 3-D image volume V_{rec} is obtained by computing the diffracted field in planes located at increasing distances from the hologram (see Fig. 3.4). Different techniques to simulate diffraction have been proposed: Fresnel transform (Kreis 2005), fractional Fourier transform (Pellat-Finet 1994; Ozaktas *et al*. 1996), wavelets transform (Liebling *et al*. 2003). Using a convolution-based diffraction model, V_{rec} is given by:

$$V_{\text{rec}}(x_p, y_q, z_r) = [D * h_{z_r}](x_p, y_q) \quad \leftrightarrow \quad \boldsymbol{v} = \boldsymbol{H}^t \boldsymbol{d}. \tag{3.7}$$

Using Eq. (3.6), $\boldsymbol{v}$ can be expressed as:

$$\boldsymbol{v} = \boldsymbol{H}^t \boldsymbol{H} \boldsymbol{\vartheta} + \boldsymbol{\epsilon} \tag{3.8}$$

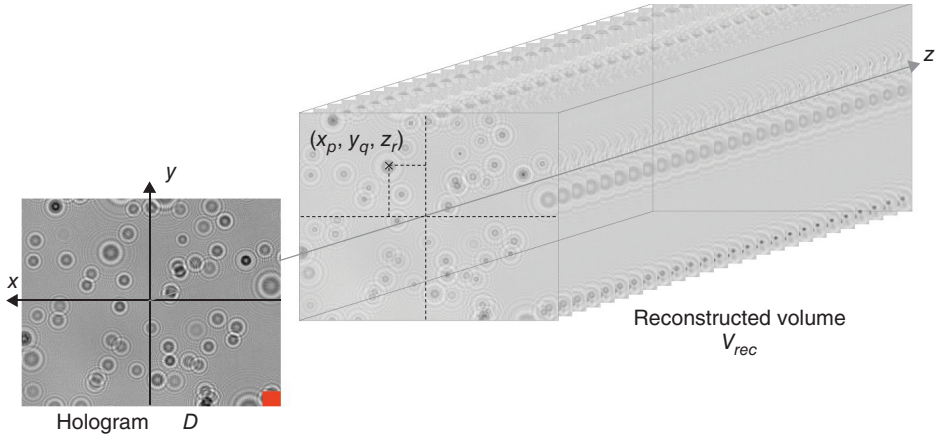

Figure 3.4 Illustration of classical reconstruction based on hologram diffraction. The z axis is magnified versus x and y axis. The red rectangle corresponds to the real size of the hologram

Unfortunately, hologram diffraction does not invert hologram recording: operator $\boldsymbol{H}^t\boldsymbol{H}$ is far from the identity (i.e., the impulse response of the system "hologram recording" + "linear reconstruction" is a spatially variant halo).

The second step consists of localizing and sizing each object in the obtained 3-D image. The best focusing plane for each object has to be detected. Various criteria are suggested in the literature. Some are based on the local analysis of the sampled reconstructed volume. For example, Murata and Yasuda (2000) searched for the minimum gray level on the z-axis crossing the object center and Malek *et al*. (2004) computed the barycenter of the labeled object image after thresholding the 3-D reconstructed image. Pan and Meng (2003) used the imaginary part of the reconstructed field. Other approaches are based on an analysis of the object's 3-D image. Liebling and Unser (2004) used the criterion of the sparsity of wavelet's coefficients and Dubois *et al*. (2006) used the minimization of the integrated reconstructed amplitude. Hologram-diffraction based approaches suffer from various limitations:

- the lateral field of view is limited and, in practice, must be restricted to the center of the reconstructed images to reduce border effects;
- under-sampled holograms can lead to artifacts in the reconstructed volume (e.g., ghost images);
- twin-images of the objects superimposed on the real image can bias the localization and sizing of the objects;
- multiple intensity peaks can occur close to the actual in-focus depth location of each object (Fournier *et al*. 2004), leading to biased measurements when searching for in-focus plane using an intensity criterion;
- several tuning parameters depending on the experiment must be adjusted by the user.

In spite of these drawbacks, this approach is successfully used for many applications due to its short processing time and to satisfying accuracy in the center of the field of view. In the next section, we present signal processing approaches to reconstruct holograms that overcome the previously mentioned limits.

3.4 Hologram Reconstruction Formulated as an Inverse Problem

In Section 3.2, two linear models of the hologram formation were described. The equation FI (Eq. 3.5) models holograms of objects that have known diffraction patterns stored in a dictionary $\boldsymbol{M}$. This is the case for simple shaped objects described by few parameters, with diffraction patterns, which are given by an analytical formula (e.g., radius and 3-D position for opaque spheres with a diffraction pattern model given by Tyler and Thompson 1976, or the Mie scattering formula, see Bohren and Huffman 2008). The non zero values of the vector $\boldsymbol{\alpha}$ give the amplitude of the diffraction patterns that are present on the hologram. Equation FII (Eq. 3.6) models the diffraction of more complex objects (i.e., non parametric objects) that can be described by their opacity distribution $\boldsymbol{\vartheta}$ sampled on a 3-D grid. The amplitude of the objects $\boldsymbol{\alpha}$ or the opacity distribution $\boldsymbol{\vartheta}$ can be estimated by inverting the hologram formation model, using a suitable regularization as typically done when dealing with ill-conditioned inverse problems.

Assuming, in our hologram models, that the noise $\boldsymbol{\epsilon}$ is Gaussian and described by an inverse covariance matrix $\boldsymbol{W}$, data are then distributed following a distribution of the form:

$$\text{(FI)} \quad \mathrm{p}(\boldsymbol{d}|\boldsymbol{\alpha}) \propto \exp\ [-(\boldsymbol{M}\ \boldsymbol{\alpha} - \boldsymbol{d})^t \boldsymbol{W}(\boldsymbol{M}\ \boldsymbol{\alpha} - \boldsymbol{d})], \tag{3.9}$$

$$\text{(FII)} \quad \mathrm{p}(\boldsymbol{d}|\boldsymbol{\vartheta}) \propto \exp\ [-(\boldsymbol{H}\ \boldsymbol{\vartheta} - \boldsymbol{d})^t \boldsymbol{W}(\boldsymbol{H}\ \boldsymbol{\vartheta} - \boldsymbol{d})]. \tag{3.10}$$

Noise is generally considered white, so that $\boldsymbol{W}$ is diagonal: $\boldsymbol{W} = \mathrm{diag}(\boldsymbol{w})$. Non uniform $\boldsymbol{w}$ can account for a signal-dependant variance. It can also be used to model missing data (e.g., $w_k = 0$ for pixels k that are outside the hologram support and $w_k = 1$ for pixels k that are inside the hologram support). Using this rigorous way to account for the limited size of the sensor permits an increase of the field-of-view size. Soulez *et al*. (2007b) showed that the field of view can be enlarged by a factor of 16. Chareyron *et al*. (2012) and Seifi *et al*. (2013b) showed that it is also possible to use such a binary mask to exclude, from the hologram analysis, some regions of the signal that cannot be explained with a simple mathematical model.

The negative log-likelihood $\mathcal{L}$ is given, up to an additive and a multiplicative constant, by:

$$\text{(FI)} \quad \mathcal{L}_{\mathrm{I}}(\boldsymbol{d}, \boldsymbol{\alpha}) = -\log\ \mathrm{p}(\boldsymbol{d}|\boldsymbol{\alpha}) = \|\boldsymbol{M}\ \boldsymbol{\alpha} - \boldsymbol{d}\|^2_{\boldsymbol{w}}, \tag{3.11}$$

$$\text{(FII)} \quad \mathcal{L}_{\mathrm{II}}(\boldsymbol{d}, \boldsymbol{\vartheta}) = -\log\ \mathrm{p}(\boldsymbol{d}|\boldsymbol{\vartheta}) = \|\boldsymbol{H}\ \boldsymbol{\vartheta} - \boldsymbol{d}\|^2_{\boldsymbol{w}}. \tag{3.12}$$

where $\|\boldsymbol{u}\|^2_{\boldsymbol{w}}$ is the weighted L_2 norm[1]. To get rid of a non perfect background removal that can leave a residual offset, we use zero mean data ($\overline{\boldsymbol{d}}$) and zero mean diffraction model ($\overline{\boldsymbol{M}}\ \boldsymbol{\alpha}$) on the hologram support. The neg-log-likelihood $\mathcal{L}$ is then given by:

$$\text{(FI)} \quad \mathcal{L}_{\mathrm{I}}(\boldsymbol{d}, \boldsymbol{\alpha}) = \|\overline{\boldsymbol{M}}\ \boldsymbol{\alpha} - \overline{\boldsymbol{d}}\|^2_{\boldsymbol{w}}, \tag{3.13}$$

$$\text{(FII)} \quad \mathcal{L}_{\mathrm{II}}(\boldsymbol{d}, \boldsymbol{\vartheta}) = \|\overline{\boldsymbol{H}}\ \boldsymbol{\vartheta} - \overline{\boldsymbol{d}}\|^2_{\boldsymbol{w}}, \tag{3.14}$$

with the zero-mean variables expressed with weighted scalar product[1]:

$$\overline{\boldsymbol{d}} = \boldsymbol{d} - \boldsymbol{1}\langle \boldsymbol{1}, \boldsymbol{d}\rangle_{\boldsymbol{w}} = \begin{bmatrix} d_1 - \sum\limits_k w_k d_k / \sum\limits_k w_k \\ \vdots \\ d_N - \sum\limits_k w_k d_k / \sum\limits_k w_k \end{bmatrix},$$

$$\overline{\boldsymbol{M}} = [\overline{\boldsymbol{m}}_1, \ \ldots\ , \overline{\boldsymbol{m}}_n],$$

$$\forall j,\ \overline{\boldsymbol{m}}_j = \boldsymbol{1}\langle \boldsymbol{1}, \boldsymbol{m}_j\rangle_{\boldsymbol{w}} - \boldsymbol{m}_j = \begin{bmatrix} \sum\limits_k w_k m_k / \sum\limits_k w_k \ - \boldsymbol{m}_1 \\ \vdots \\ \sum\limits_k w_k m_k / \sum\limits_k w_k \ - m_N \end{bmatrix},$$

[1]

$$\text{weighted scalar product is defined as: } \langle \boldsymbol{u}, \boldsymbol{v}\rangle_{\boldsymbol{w}} = \frac{\sum\limits_k w_k u_k v_k}{\sum\limits_k w_k}$$

$$\text{weighted } L_2 \text{norm is defined as: } \|\boldsymbol{u}\|^2_{\boldsymbol{w}} = \langle \boldsymbol{u}, \boldsymbol{u}\rangle_{\boldsymbol{w}} = \frac{\sum\limits_k w_k u_k^2}{\sum\limits_k w_k}$$

$$\overline{\boldsymbol{H}} = [\overline{\mathbf{h}}_{z_1}, \ \ldots \ , \overline{\mathbf{h}}_{z_K}],$$

$$\forall k, \ \overline{\mathbf{h}}_k = \boldsymbol{1}\langle \boldsymbol{1}, \mathbf{h}_k \rangle_{\boldsymbol{w}} - \mathbf{h}_k = \begin{bmatrix} \sum_k w_k h_k / \sum_k w_k \ - h_1 \\ \vdots \\ \sum_k w_k h_k / \sum_k w_k \ - h_{N^2} \end{bmatrix}.$$

When the objects can be parameterized (e.g., disks), they are detected and localized using form (FI), as detailed in Section 3.4.1. More complex objects require the reconstruction of the opacity distribution using form (FII), see Section 3.4.2.

3.4.1 Reconstruction of Parametric Objects (FI)

The hologram model of objects that can be described with few parameters (e.g., 3-D location, shape, optical index,...), is also parametric. It can be used to create a dictionary $\boldsymbol{M}$ of diffraction patterns to model the hologram as a linear summation of the dictionary elements (form FI). Since the 3-D location of an object is continuous, the dictionary $\boldsymbol{M}$ should also be continuous (i.e., with infinite elements). The problem then amounts to finding the best match (least squares solution) between a linear summation of diffraction pattern models and the captured hologram. Several authors already suggest fitting models to the hologram leading to accurate and impressive results (Lee *et al*. 2007; Cheong *et al*. 2010; Fung *et al*. 2011; Cheong *et al*. 2011). However, they use a starting point for a fitting algorithm that is provided by the user or by a segmentation of the back propagated field that can be biased (e.g., for out-of-classical field objects) and requires tuning parameters.

Our approach, proposed in Soulez *et al*. (2007a,b), leads to an unsupervised algorithm and makes possible object reconstruction out of the classical field of view. It solves the problem iteratively, that is, objects are detected one after the other, aiming in each iteration to find the best fit between the model and the hologram. It consists of three steps:

- A *global detection step* (or a coarse estimation step), which finds the best-matching element in a discrete dictionary $\boldsymbol{M}$ (i.e., the diffraction pattern for a given 3-D location and shape). It is also called the *exhaustive search step*.
- A *local optimization step* (or a refinement step), which fits the selected diffraction pattern to the data for sub-pixel estimation.
- A *cleaning step*, which subtracts the detected pattern from the hologram to increase the signal-to-noise ratio of the remaining objects.

The procedure is then repeated on the residuals until no more object is detected. This approach to hologram reconstruction corresponds to the class of greedy algorithms (Denis *et al*. 2009a) known in signal processing as the *Matching Pursuit* (Mallat and Zhang 1993), or in radio-astronomy as the CLEAN algorithm (Högbom 1974).

3.4.1.1 Global object detection

In the first step, the best matching diffraction pattern of a sampled dictionary $\boldsymbol{M}$ is searched. The element that leads to the largest decrease of the neg-log-likelihood $\mathcal{L}_{\mathrm{I}}$ is identified as the

most probable (i.e., detected):

$$\underset{\substack{\alpha \geq 0 \\ \overline{m} \in \{\overline{m}_1, \ldots, \overline{m}_n\}}}{\arg\min} \; \|\alpha\, \overline{m} - \overline{d}\|_w^2. \tag{3.15}$$

By replacing α by its optimal value in Eq. (3.15), the diffraction pattern $\overline{m}^\dagger$ that minimizes $\mathcal{L}_\mathrm{I}$ is also the one that maximizes the criterion $C(\overline{m})$ (Soulez *et al*. 2007b):

$$\overline{m}^\dagger = \underset{\overline{m} \in \{\overline{m}_1, \ldots, \overline{m}_n\}}{\arg\max} \; C(\overline{m}) \qquad \text{subject to} \qquad \langle \overline{m}, \overline{d} \rangle_w \geq 0, \tag{3.16}$$

$$\text{with} \quad C(\overline{m}) = \frac{\langle \overline{m}, \overline{d} \rangle_w^2}{\|\overline{m}\|_w^2}. \tag{3.17}$$

The detected object is the one whose diffraction pattern has the highest correlation with the data: $C(\overline{m})$ corresponds to the square of a weighted normalized correlation between a model

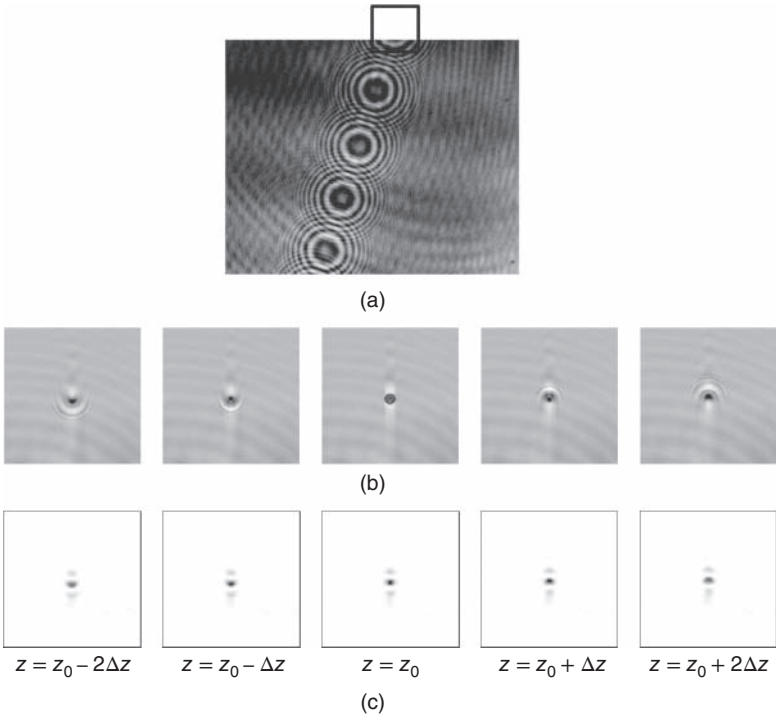

Figure 3.5 Illustration of classical reconstruction compared with the criterion map: (a) experimental in-line hologram of droplets (b) classical reconstruction based on hologram diffraction at different depths z. Artifacts appear during the numerical reconstruction due to the truncation of diffraction rings on the hologram boundary. (c) Criterion computation based on "Inverse Problems" approach at different depths z (see Eq. 3.17). For the sake of visualization, the contrast is inversed. The images represented in (b) and (c) correspond to the square area drawn on the hologram (a). $z_0 = 0.273$ m corresponds to the in-focus distance, $\Delta z = 6$ mm

and the hologram. Since the diffraction patterns are shift-invariant, Soulez *et al*. (2007b) show that the correlations in Eq. (3.16) can be computed using fast Fourier transforms.

Note that Gire *et al*. (2008) show that this global detection is less sensitive to ghost images compared with the classical reconstruction. Furthermore, "Border effects", which classically lead to measurement bias, are removed by taking into account the boundaries of the sensor by means of a binary mask $\boldsymbol{w}$. Figure 3.5(c) shows the values of the criterion $C(\overline{\boldsymbol{m}})$ on several consecutive reconstructed planes (for the sake of visualization, the contrast is inversed). Unlike in classical reconstruction, the maximum criterion value in these planes is on the in-focus plane.

3.4.1.2 Local optimization

The global detection step gives a rough estimation of the objects parameters. In the local optimization step these parameters are used as the first guess of an optimization algorithm to get sub-pixel accuracy.

Figures 3.6 and 3.7 illustrate an application of this algorithm to detect spherical droplets.

3.4.1.3 Cleaning

Once the local optimization step is finished, the accurate estimated parameters are used to simulate the diffraction pattern and remove it from the data.

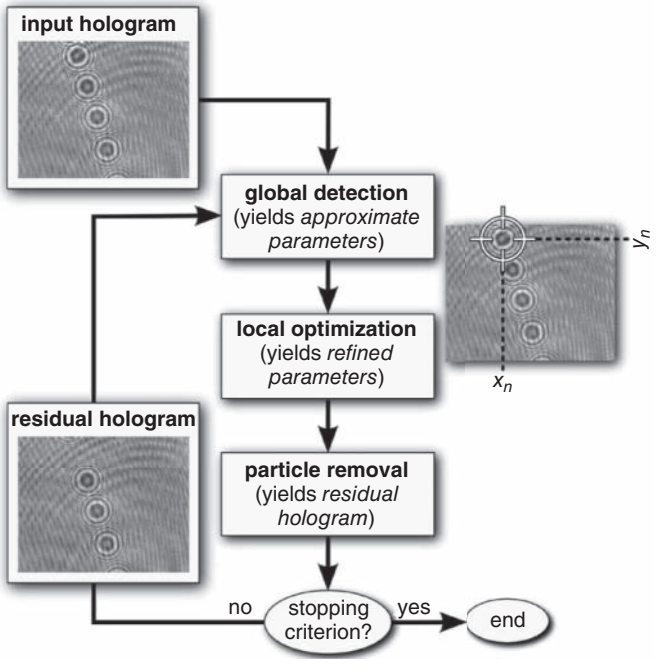

Figure 3.6 Iterative algorithm to estimate the parameters of objects distributed in a volume. *Source*: Soulez F., Denis L., Thiebaut E., Fournier C., and Goepfert C., 2007b. Reproduced with permission from the Optical Society

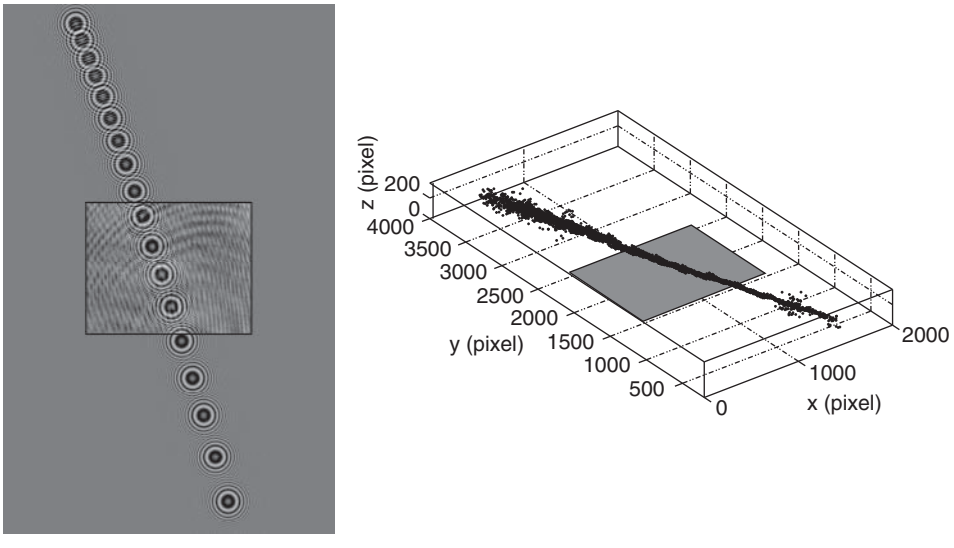

Figure 3.7 Illustration of droplets detection located out-of-field (from Soulez *et al*. 2007b): (a) superimposition of one hologram of the series and the model of this hologram calculated from 16 detected particles (including 12 out-of-field); (b) represents the 3-D jet obtained by the detection of all particles located in a field equal to more than 16 times the hologram surface. The corresponding surface of the sensor is represented by a gray rectangle. The droplet detection is realized without significant bias, even for particles located far away from the sensor. *Source*: Soulez F, Denis L, Thiebaut E, Fournier C and Goepfert C 2007b. Reproduced with permission from the Optical Society

Repeating the detection, localization, and cleaning steps on the residual signal improves the signal-to-noise ratio of remaining objects with fainter signatures, in particular, particles distant from the camera center, and prevents from detecting the same particle multiple times. An illustration of cleaning is shown on Fig. 3.8 and on a video.

The algorithm stops when no more reliable particle can be detected ($\alpha < 0$). This algorithm is implemented in an online free Matlab toolbox called "HoloRec3D".[2]

This greedy algorithm was used by Soulez *et al*. (2007a,b) to 3-D reconstruct water droplets accurately, behaving as opaque spheres with diameters of about 100 µm. Grier's team used a simple model fitting algorithm and a Lorentz Mie Theory hologram formation model to reconstruct colloidal spherical particles and their optical index with diameters of about 1 µm (Lee *et al*. 2007; Cheong *et al*. 2010).

3.4.2 Reconstruction of 3-D Transmittance Distributions (FII)

When the objects are too complex to be parameterized by few parameters, or when the purpose is to reconstruct unknown objects, form (FII) is considered: an opacity distribution sampled on a 3-D grid is reconstructed from the hologram. Due to the ill-posed nature of this inversion

[2] http://labh-curien.univ-st-etienne.fr/wiki-reconstruction/index.php

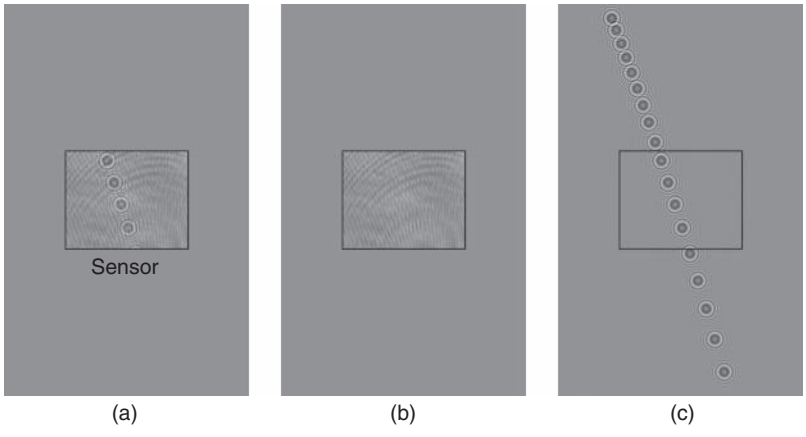

Figure 3.8 Illustration of the cleaning step: (a) experimental hologram, (b) cleaned hologram, and (c) simulated hologram using the estimated parameters

problem, it is mandatory to regularize it. The reconstructed 3-D distribution $\boldsymbol{\vartheta}$ is then given by the *Maximum A Posteriori* estimate (MAP):

$$\boldsymbol{\vartheta}^{(\mathrm{MAP})} = \arg\min_{\boldsymbol{\vartheta}} \quad \|\overline{\boldsymbol{H}}\boldsymbol{\vartheta} - \overline{\boldsymbol{d}}\|_w^2 + \beta\, \Phi_{\mathrm{reg}}(\boldsymbol{\vartheta}). \tag{3.18}$$

Several regularizations Φ_{reg} have been proposed to reconstruct holograms. When extended objects are considered, an edge-preserving smoothness prior, like total variation (the sum of the spatial gradient norm), is generally chosen (see Sotthivirat and Fessler 2004; Brady *et al*. 2009; Marim *et al*. 2010, 2011):

$$\boldsymbol{\vartheta}^{(\mathrm{MAP})} = \arg\min_{\boldsymbol{\vartheta}} \quad \|\overline{\boldsymbol{H}}\boldsymbol{\vartheta} - \overline{\boldsymbol{d}}\|_{\boldsymbol{w}}^2 + \beta \mathrm{TV}(\boldsymbol{\vartheta}),$$

$$\text{with} \qquad \mathrm{TV}(\boldsymbol{\vartheta}) = \sum_k \sqrt{(\boldsymbol{D}_{\mathbf{x}}\ \boldsymbol{\vartheta})_k^2 + (\boldsymbol{D}_{\mathbf{y}}\ \boldsymbol{\vartheta})_k^2},$$

where $\boldsymbol{D}_{\mathbf{x}}$ and $\boldsymbol{D}_{\mathbf{y}}$ are the finite difference operators along x and y (i.e., tranversal) axes.

Denis *et al*. (2009b) showed that enforcing a sparsity constraint through an ℓ^1 norm is sufficient to reconstruct holograms of diluted volumes:

$$\boldsymbol{\vartheta}^{(\mathrm{MAP})} = \arg\min_{\boldsymbol{\vartheta}} \quad \|\overline{\boldsymbol{H}}\boldsymbol{\vartheta} - \overline{\boldsymbol{d}}\|_{\boldsymbol{w}}^2 + \beta\, \|\boldsymbol{\vartheta}\|_1, \qquad \text{with} \qquad \|\boldsymbol{\vartheta}\|_1 = \sum_k |\vartheta_k|. \tag{3.19}$$

A positivity constraint and spatially-variant regularization weights $\Phi_{\mathrm{reg}}(\boldsymbol{\vartheta}) = \sum_k \beta_k |\vartheta_k|$ improve the reconstruction and make it possible to extend the field of view, as illustrated in Fig. 3.9.

Note that the ℓ^1 norm minimization can also be applied to the object detection problem described in the previous section. Joint detection of all objects is more robust in the case of many objects than iterative detection of one object at a time. Intermediate procedures have been proposed in the compressed sensing literature (Needell and Tropp 2009) that detect several objects at a time, in a greedy fashion, and which can be adapted to include the local optimization step used to model a continuous dictionary.

Figure 3.9 Reconstruction of an experimental Gabor hologram of a glass reticle (from Denis *et al*. 2009b): hologram (*left*); classical linear reconstruction (*center*); MAP estimate with sparsity enducing prior to Eq. (3.19) and positivity constraint (*right*). Regularized reconstruction of holograms makes it possible to extend the field the view and suppresses twin-image artifacts. *Source*: Denis L, Lorenz D, Thiebaut E, Fournier C and Trede D 2009b. Reproduced with permission from the Optical Society

3.5 Estimation of Accuracy

The estimation and the improvement of accuracy are key issues in DH. (Jacquot *et al*. 2001; Stern and Javidi 2006; Garcia Sucerquia *et al*. 2006; Kelly *et al*. 2009). As the accuracy depends on several experimental parameters (e.g., sensor definition, fill factor, and recording distance) experimenters are in need of criteria to tune the experimental setup and to select the reconstruction algorithm that will provide the best achievable accuracy. The commonly used approach for accuracy estimation is to evaluate the Rayleigh resolution by estimating the width of the point spread function of the digital holographic system in the reconstructed planes. Fournier *et al*. (2010) suggested a methodology based on parametric estimation theory (see Kay 2008) to estimate the single point resolution defined in Dekker and den Bos (1997) (i.e., the standard deviation of the 3-D coordinates of a point source) in on-axis DH. This methodology can be applied to many DH configurations by adapting the hologram formation model, and possibly changing the noise model.

According to Cramér–Rao inequality, the covariance matrix of any unbiased estimator $\hat{\boldsymbol{\theta}} = \{\hat{\theta}_i\}_{i=1:n_p}$ of the unknown vector parameter θ^* is bounded from below by the inverse of the so-called Fisher information matrix:

$$var(\hat{\theta}_i) \geq [\boldsymbol{I}^{-1}(\boldsymbol{\theta}^*)]_{i,i}, \tag{3.20}$$

where $\boldsymbol{I}(\boldsymbol{\theta}^*)$ is the $n_p \times n_p$ Fisher information matrix.

The Fisher information matrix is defined from the gradients of the log-likelihood function $\log\, p(\boldsymbol{d};\theta)$ (Kay 2008):

$$[\boldsymbol{I}(\boldsymbol{\theta})]_{i,j} \underset{=}{\text{def}} E\left[\frac{\partial \log\, p(\boldsymbol{d};\boldsymbol{\theta})}{\partial \boldsymbol{\theta}_i}\frac{\partial \log\, p(\boldsymbol{d};\boldsymbol{\theta})}{\partial \theta_j}\right], \tag{3.21}$$

where $\boldsymbol{\theta}$ stands for the parameters vector of the object (e.g., (x, y, z, r) for a sphere located at (x, y, z) of radius r).

In the case of additive white Gaussian noise model (see Section 3.4.1), Fisher information matrix can be computed using gradients of the model $m(\theta)$ (Fournier *et al*. 2010):

$$[\boldsymbol{I}(\boldsymbol{\theta})]_{i,j} = \alpha^2 \left\langle \frac{\partial \boldsymbol{m}(\boldsymbol{\theta})}{\partial \theta_i}, \frac{\partial \boldsymbol{m}(\boldsymbol{\theta})}{\partial \theta_j} \right\rangle_{\boldsymbol{w}}. \tag{3.22}$$

Note that $\boldsymbol{w}$, as in the reconstruction algorithms, accounts for the finite sensor support size or for excluded data region of the analysis. The Cramér–Rao lower bound (CRLB) is asymptotically (for large samples) reached by maximum likelihood estimators. In digital holography, where the signal is distributed on the whole sensor, estimation is performed using a large set of independent identically distributed measurements (typically more than one million). The maximum likelihood estimator then approaches the CRLB. Note that if the optimization technique used for maximization of the likelihood fails to reach the global minimum, or if the noise level is too high, the resulting estimation error will exceed CRLB.

In a previous study (Fournier *et al*. 2010) about single point resolution estimation, we presented closed-form expressions of resolutions. It showed that:

- the CRLB predicted resolution behaves on optical axis as the classical Rayleigh resolution predicts;
- the CRLB give the resolution out of the optical axis and even out of the classical field of view;
- estimated parameters are correlated (an error on one parameter influences the estimation of the others).

Examples of standard deviation maps calculated using the described methodology are presented in Fig. 3.10 (Plate 5).

3.6 Fast Processing Algorithms

Reducing the processing time is one of the main issues in digital holography. One way to fix it is to use hardware device (e.g., Graphics Processing Units or multiprocessors: see Ahrenberg *et al*. 2009, Shimobaba *et al*. 2008, Page *et al*. 2008). A second way is to decrease the complexity of the algorithms. We worked on the latter issue tackling the time processing bottleneck of the global detection step in parametric object reconstruction (see 3.4.1). We present, in this section, two of our contributions aimed at reducing the complexity of this step while preserving the optimality of the signal processing approach.

3.6.1 Multiscale Algorithm for Reconstruction of Parametric Objects

Considering parametric objects described by n_θ parameters (e.g., 3-D position and intrinsic parameters such as radius, optical index etc.), the exhaustive-search step requires a time consuming exploration of the sampled parameter space of n_θ dimensions. Let us consider the

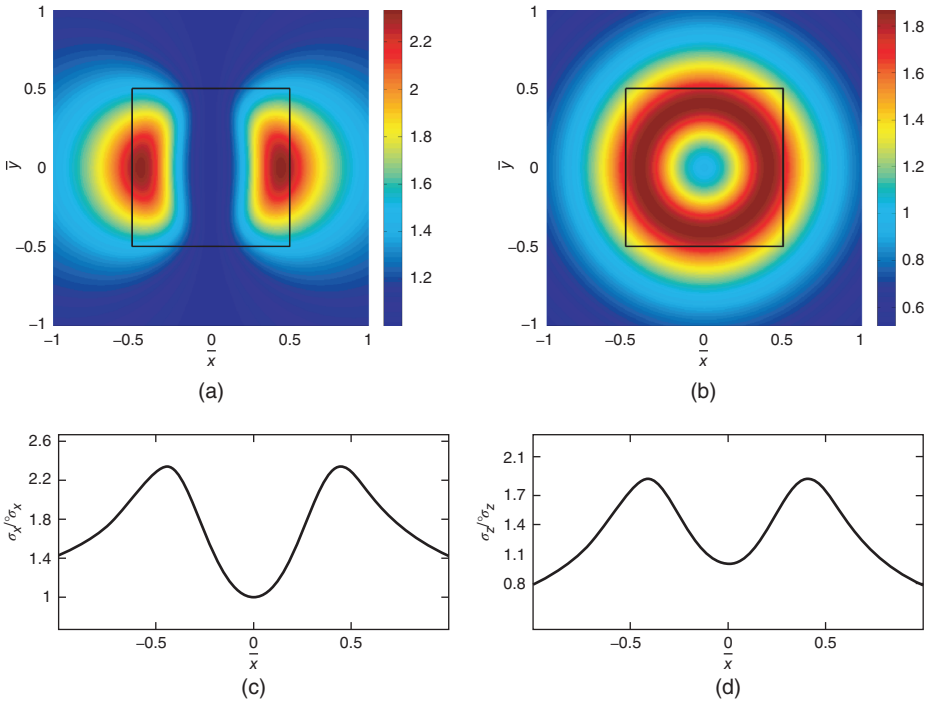

Figure 3.10 (Plate 5) Single point resolution in a transversal plane (from Fournier *et al*. 2010): (a) x-resolution map normalized by the value of x-resolution on the optical axis; (b) normalized z-resolution map; (c) x-resolution for $\overline{y} = 0$; (d) z-resolution for $\overline{y} = 0$; for $z = 100$ mm, $\lambda = 0.532$ µm, $\Omega = 8.6.10^{-3}$ and $SNR = 10$. The squares in the center of figures (a) and (b) represent the sensor boundaries. *Source*: Fournier C, Denis L and Fournel T 2010. Reproduced with permission from the Optical Society. *See plate section for the color version*

simple case of spherical opaque objects with only four parameters (i.e., (x, y, z, r) 3-D coordinates, and radius). The search step is performed in 4-D space. To reach pixel-accuracy in (x, y) and sufficient accuracy in other parameters, hundreds of (z, r) pairs may need to be considered for each (x, y) location, leading to hundreds of millions or billions of quadruples (x, y, z, r) to be tested. Shift-invariance of the model can be exploited by using the Fast Fourier Transforms (FFT). The search is thus reduced for each exhaustive-search step to the computation of hundreds of convolutions to evaluate the generalized maximum correlation criterion given in 3.17 (the criterion requires 7 FFTs for each (z, r) pair (Soulez *et al*. 2007b). This is then repeated for each object unless multiple object detection is implemented (Needell and Tropp 2009). The main feature of the multiscale algorithm is to replace the computationally intensive exhaustive search by coarse-to-fine processing. The exhaustive search is carried out only on a down-sampled version of the hologram.

A sketch of the algorithm is illustrated in Fig. 3.11 (for more detail please refer to Seifi *et al*. 2013a). Since exhaustive search is a computational bottleneck, we build a multi-resolution

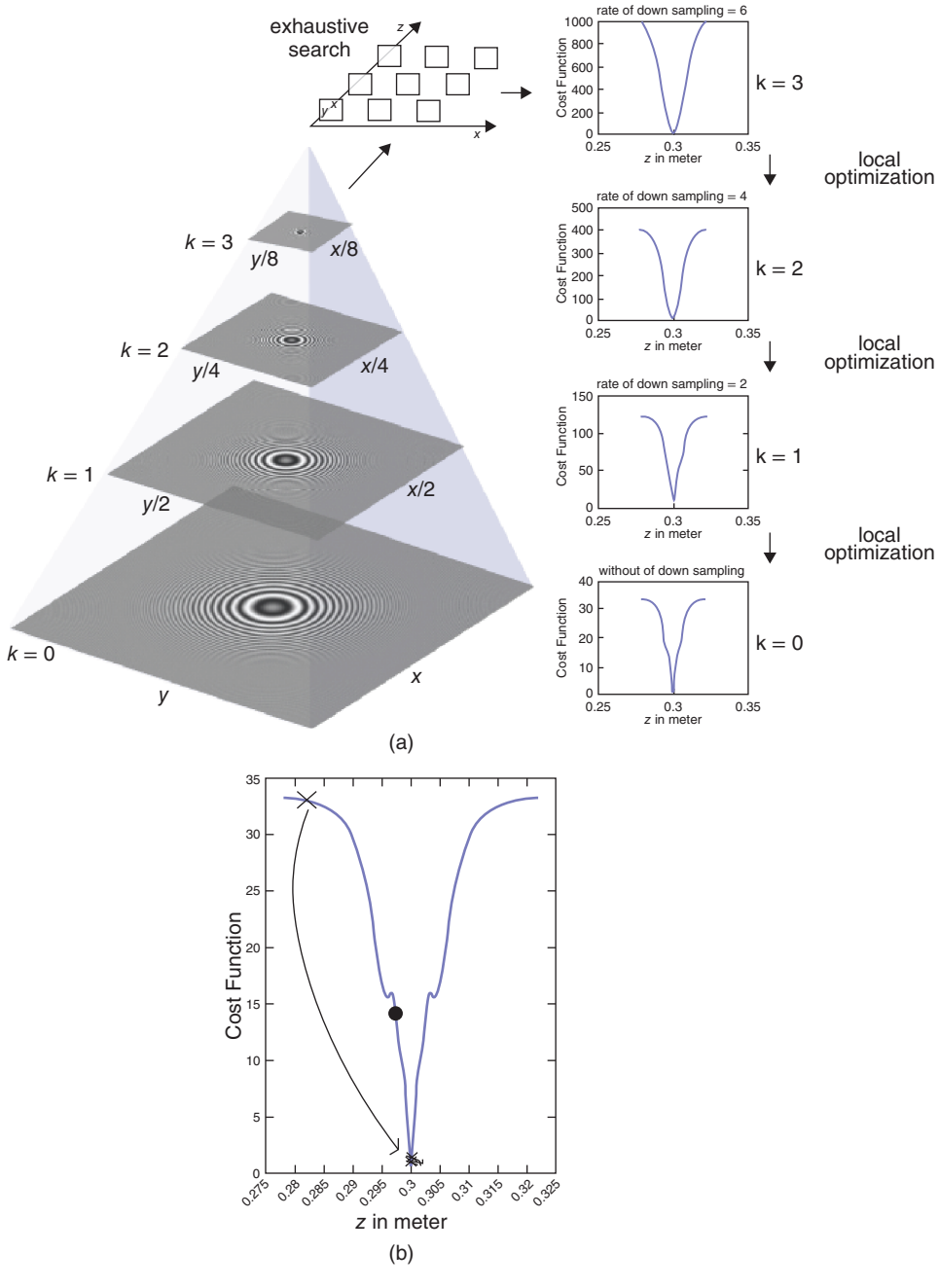

Figure 3.11 (a) Schema of the proposed multiscale algorithm, (b) 1-D profile of the cost function computed on the original hologram: the black crosses show the results of the estimation after each step of pyramidal multiscale algorithm on the profile of the cost function, the black circle shows an example of a coarse estimation from exhaustive search in the single-scale approach ($k = 0$). *Source*: Seifi M, Fournier C, Denis L, Chareyron D and Marie JL 2012. Reproduced with permission from the Optical Society

pyramid from the hologram and perform an exhaustive search only on the coarsest scale. Local optimization is then performed on increasingly fine scales, restarting numerical optimization each time from the parameters obtained at the previous (coarser) scale. The down-sampled hologram at level k is computed by low-pass filtering and downsampling the full-resolution hologram $\boldsymbol{d}$ by a linear filter. Using a coarse resolution hologram for the exhaustive search step not only reduces the number of (x, y) samples by a factor proportional to the layer number but also makes the log-likelihood smoother. Sampling of parameters z and r (i.e., depth and radius of a particle) can also be made coarser in this way. Figure 3.11(a) illustrates the widening of cost function when coarser resolution holograms are considered (for the sake of illustration a profile of the cost function along axis z is drawn). The risk of getting trapped in a local minimum is then much weaker. This fact relaxes sampling constraints that guarantee the estimation to be within reach of the global minimum.

The processing time gain depends on two main factors: the maximum downsampling period that can be used and the stopping criteria of the iterative optimization operations. The maximum downsampling period is chosen considering that a minimum number of fringes should remain on the coarsest downsampled hologram. The criterion for stopping the optimization process is given by the CRLB estimation for each resolution of the pyramid. Indeed, the optimization can be stopped when the parameters changes are equal to the theoretical standard deviations. We have validated our algorithm using a collection of simulated holograms and real holograms. The results indicate a factor of four increase in speed for a three-layer multiscale pyramid.

An other advantage of the proposed coarse-to-fine approach is that it provides an early estimation of parameters with additional accuracy after each refinement step. These coarse results can provide a quick feedback for huge stacks of holograms generated by high-speed cameras while off-line processes can refine the estimations using the finer scales.

3.6.2 Dictionary Size Reduction for Fast Global Detection

Direct matching of diffraction patterns on the in-line holograms dramatically improves the quality of reconstructed images, as discussed in Sections 3.4 and 3.5. Reconstruction methods dedicated to parametric objects (form FI described in Section 3.4.1) can be extended to a larger class of objects by considering the collection (or dictionary) of all objects of interest $\boldsymbol{C}$. Matrix $\boldsymbol{C}$ is formed by collecting columns $\boldsymbol{c}_i$, each representing a different object. If the dictionary is large enough (i.e., if $\boldsymbol{C}$ has many columns), any object of the considered class can be well approximated by its closest representative $\boldsymbol{c}_i$.

Objects are not directly observed in holography, only their diffraction patterns are captured. Object recognition can then be performed in the framework of inverse problems by matching diffraction patterns. The dictionary of all possible diffraction patterns $\overline{\boldsymbol{M}}$ introduced in Section 3.4.1 is obtained by considering for each object $\boldsymbol{c}_i$ diffraction patterns at various distances and all possible (x, y) translations. Let $\boldsymbol{K}$ be the dictionary of geometrically-centered diffraction patterns, that is, the collection of the diffraction patterns for all objects, at all considered depths, for objects centered on the optical axis. Dictionary $\boldsymbol{K}$ captures the variability of diffraction patterns of different objects with different recording distances. Due to object variability (the number of columns of dictionary $\boldsymbol{C}$) and depth range, the dictionary of diffraction patterns $\boldsymbol{K}$ may be very large. Direct application of the greedy algorithm described in Section 3.4.1 would then lead to prohibitive computation time.

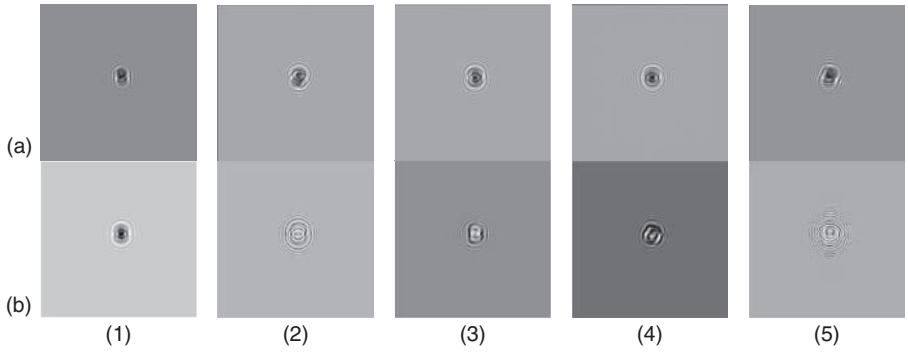

Figure 3.12 (a) Five random patterns of a 600-pattern dictionary and (b) the first five modes of the same dictionary. Patterns of the dictionary are calculated respectively for: (a-1) a "1" placed at 0.15 m from sensor, (a-2) a "2" placed at 0.1583 m, (a-3) a "3" placed at 0.1683 m, (a-4) a "6" placed at 0.1817 m, (a-5) a "7" placed at 0.19 m. The sensor is a 400×400 pixel camera with a fill-factor of 0.7 and a pixel size of 20 μm. The wavelength of the illuminating laser beam is 0.532 μm. The depth range of patterns in the dictionary is [0.15 m, 0.2 m]

Diffraction patterns in dictionary $\boldsymbol{K}$ exhibit various degrees of correlation and most of their variability can be captured in a low-dimensional sub-space:

$$\boldsymbol{K} \approx \sum_{i=1}^{t} \boldsymbol{u}_i \sigma_i \boldsymbol{v}_i^{\mathrm{t}} , \tag{3.23}$$

where $\boldsymbol{K}$ is approximated by the best rank-t matrix as obtained by the singular value decomposition (SVD) considering the singular vectors $\boldsymbol{u}_i$ and $\boldsymbol{v}_i$ associated with the t largest singular values $\{\sigma_1, \ldots, \sigma_t\}$. Within this approximation, diffraction pattern $\boldsymbol{k}_j$ is represented by the linear combination $\sum_i \beta_{i,j} \boldsymbol{u}_i$, where coefficient $\beta_{i,j}$ is equal to $\sigma_i \boldsymbol{v}_i(j)$. Vectors $\boldsymbol{u}_i$ represent so-called modes of the diffraction-patterns.

Using this approximation, the correlation terms in Eq. (3.17) are approximated as a linear combination of the correlation of each of the t modes with the data:

$$\langle \boldsymbol{k}_j, \overline{\boldsymbol{d}} \rangle_w \approx \sum_{i=1}^{t} \beta_{i,j} \langle \boldsymbol{u}_i, \overline{\boldsymbol{d}} \rangle_w . \tag{3.24}$$

In Eq. (3.24), the scalar product $\langle \boldsymbol{u}_i, \overline{\boldsymbol{d}} \rangle_w$ does not depend on the considered diffraction-pattern $\boldsymbol{k}_j$ and can thus be computed once for all the diffraction-patterns. For more details, please refer to Seifi *et al*. (2013a).

3.7 Conclusion

Digital holography is very efficient for quantitative 3-D tracking and sizing of high speed objects spread in a volume. Classical reconstruction methods, based on back-propagation, have been used successfully since the 1980s to perform 3-D reconstructions. However, image processing techniques based on signal processing approaches and aiming to invert the image

formation have been used increasingly in recent years to achieve accurate 3-D reconstruction. These approaches provide a rigorous way to process on-axis holograms. They lead, in certain cases, to optimal image processing so that their accuracy gets close to the Cramér–Rao lower bound. By processing the hologram directly, they also get rid of all sources of bias appearing when simulating the back-propagation of the hologram. In this framework, our team proposed two reconstruction algorithms dedicated to two types of objects: simple shape parametric objects and sparse object fields. These algorithms lead to accurate reconstruction and enlargement of the field of view. Let us note that the algorithm dedicated to parametric objects reconstruction is unsupervised and the one dedicated to the reconstruction of sparse field object opacity distribution requires only tuning of a single hyper-parameter. However, the processing time of inverse problems algorithms can be huge when the parameters to reconstruct are numerous. To tackle this drawback one can use dedicated hardware acceleration and/or decrease the complexity of the algorithms. Recently, we suggested two algorithms with reduced complexity: a coarse-to-fine algorithm based on a multiscale resolution pyramid and an algorithm aiming to reduce the diffraction-pattern dictionary (Fig. 3.12). We expect strong development and generalization of this new family of algorithms based on inverse approaches. Some current issues are the optic modeling of image-hologram formation for some specific objects and the reduction of the algorithm's complexity.

References

Ahrenberg L, Page AJ, Hennelly BM, McDonald JB and Naughton TJ 2009 Using commodity graphics hardware for real-time digital hologram view-reconstruction. *J. Display Technol* **5**, 111–119.

Allier CP, Hiernard G, Poher V and Dinten JM 2010 Bacteria detection with thin wetting film lensless imaging. *Biomedical Optics Express* **1**(3), 762–770.

Bohren CF and Huffman DR 2008 *Absorption and Scattering of Light by Small Particles*. Wiley-VCH Verlag, Weinheim.

Brady DJ, Choi K, Marks DL, Horisaki R and Lim S 2009 Compressive holography. *Optics Express* **17**(15), 13040–13049.

Chareyron D, Marie JL, Fournier C, Gire J, Grosjean N, Denis L 2012 Testing an in-line digital holography "inverse method" for the Lagrangian tracking of evaporating droplets in homogeneous nearly isotropic turbulence. *New Journal of Physics* **14**(4), 043039.

Cheong FC, Krishnatreya BJ and Grier DG 2010 Strategies for three-dimensional particle tracking with holographic video microscopy. *Optics Express* **18**(13), 13563–13573.

Cheong FC, Xiao K, Pine DJ and Grier DG 2011 Holographic characterization of individual colloidal spheres' porosities. *Soft Matter* **7**(15), 6816–6819.

Coupland J and Lobera J 2008 Special issue: Optical tomography and digital holography. *Measurement Science and Technology* **19**(7), 070101.

Dekker AJD and den Bos AV 1997 Resolution: a survey. *Journal of the Optical Society of America A* **14**(3), 547–557.

Denis L, Lorenz D and Trede D 2009a Greedy solution of ill-posed problems: error bounds and exact inversion. *Inverse Problems* **25**, 115017.

Denis L, Lorenz D, Thiébaut E, Fournier C and Trede D 2009b Inline hologram reconstruction with sparsity constraints. *Optics Letters* **34**(22), 3475–3477.

Dubois F, Schockaert C, Callens N and Yourassowsky C 2006 Focus plane detection criteria in digital holography microscopy by amplitude analysis. *Optics Express* **14**(13), 5895–5908.

El Mallahi A, Minetti C and Dubois F 2013 Automated three-dimensional detection and classification of living organisms using digital holographic microscopy with partial spatial coherent source: application to the monitoring of drinking water resources. *Applied Optics* **52**(1), A68–A80.

Faulkner HML and Rodenburg JM 2004 Movable aperture lensless transmission microscopy: a novel phase retrieval algorithm. *Physical Review Letters* **93**(2), 23903.

Fienup JR 2010 Coherent lensless imaging *Imaging Systems* Topical Meeting, Tucson, AZ, June 7–10.

Fournier C, Denis L and Fournel T 2010 On the single point resolution of on-axis digital holography. *Journal of the Optical Society of America A* **27**(8), 1856–1862.

Fournier C, Ducottet C and Fournel T 2004 Digital in-line holography: influence of the reconstruction function on the axial profile of a reconstructed particle image. *Measurement Science & Technology* **15**, 1–8.

Fung J, Martin KE, Perry RW, Kaz DM, McGorty R and Manoharan VN 2011 Measuring translational, rotational, and vibrational dynamics in colloids with digital holographic microscopy. *Optics Express* **19**(9), 8051–8065.

Garcia-Sucerquia J, Xu W, Jericho SK, Klages P, Jericho MH and Kreuzer HJ 2006 Digital in-line holographic microscopy. *Applied Optics* **45**(5), 836–850.

Gire J, Denis L, Fournier C, Thiébaut E, Soulez F and Ducottet C 2008 Digital holography of particles: benefits of the "inverse problem" approach. *Measurement Science and Technology* **19**, 074005.

Goodman JW 1996 *Introduction to Fourier Optics: Electrical and Computer Engineering.* McGraw-Hill.

Högbom JA 1974 Aperture synthesis with a non-regular distribution of interferometer baselines. *Astronomy and Astrophysics Supplement Series* **15**, 417.

Huang B, Wang W, Bates M and Zhuang X 2008 Three-dimensional super-resolution imaging by stochastic optical reconstruction microscopy. *Science* **319**(5864), 810–813.

Jacquot M, Sandoz P and Tribillon G 2001 High resolution digital holography. *Optics Communications* **190**(1–6), 87–94.

Kay SM 2008 *Fundamentals of Statistical signal Processing: Estimation Theory* 12th edn. Prentice Hall.

Kelly DP, Hennelly BM, Pandey N, Naughton TJ and Rhodes WT 2009 Resolution limits in practical digital holographic systems. *Optical Engineering* **48**, 095801–1,095801–13.

Kim MK, Hayasaki Y, Picart P and Rosen J 2013 Digital holography and 3D imaging: introduction to feature issue. *Appl. Opt.* **52**(1), DH1.

Kreis TM 2005 *Handbook of Holographic Interferometry, Optical and Digital Methods*. Wiley-VCH Verlag, Berlin.

Lamadie F, Bruel L and Himbert M 2012 Digital holographic measurement of liquid-liquid two-phase flows. *Optics and Lasers in Engineering* **50**, 1716–1725.

Lee SH, Roichman Y, Yi GR, Kim SH, Yang SM, van Blaaderen A, *et al*. 2007 Characterizing and tracking single colloidal particles with video holographic microscopy. *Optics Express* **15**(26), 18275–18282.

Liebling M and Unser M 2004 Autofocus for digital fresnel holograms by use of a Fresnelet-sparsity criterion. *Journal of the Optical Society of America A* **21**(12), 2424–2430.

Liebling M, Blu T and Unser M 2003 Fresnelets: new multiresolution wavelet bases for digital holography. *Image Processing, IEEE Transactions on* **12**(1), 29–43.

Lim S, Marks DL and Brady DJ 2011 Sampling and processing for compressive holography [invited]. *Applied Optics* **50**(34), H75–H86.

Malek M, Allano D, Coetmellec S, Ozkul C and Lebrun D 2004 Digital in-line holography for three-dimensional-two-components particle tracking velocimetry. *Measurement Science & Technology* **15**(4), 699–705.

Mallat SG and Zhang Z 1993 Matching pursuits with time-frequency dictionaries. *Signal Processing, IEEE Transactions on* **41**(12), 3397–3415.

Marim M, Angelini E, Olivo-Marin JC and Atlan M 2011 Off-axis compressed holographic microscopy in low-light conditions. *Optics Letters* **36**(1), 79–81.

Marim MM, Atlan M, Angelini E and Olivo-Marin JC 2010 Compressed sensing with off-axis frequency-shifting holography. *Optics Letters* **35**(6), 871–873.

Moon I, Anand A, Cruz M and Javidi B 2013 Identification of malaria infected red blood cells via digital shearing interferometry and statistical inference. *IEEE Photonics Journal* **5**(5) DOI: 10.1109/JPHOT.2013.2278522.

Murata S and Yasuda N 2000 Potential of digital holography in particle measurement. *Optics and Laser Technology* **32**(7–8), 567–574.

Needell D and Tropp JA 2009 CoSaMP: iterative signal recovery from incomplete and inaccurate samples. *Applied and Computational Harmonic Analysis* **26**(3), 301–321.

Ozaktas HM, Arikan O, Kutay MA and Bozdagt G 1996 Digital computation of the fractional Fourier transform. *Signal Processing, IEEE Transactions on* **44**(9), 2141–2150.

Page AJ, Ahrenberg L and Naughton TJ 2008 Low memory distributed reconstruction of large digital holograms. *Optics Express* **16**(3), 1990–1995.

Pan G and Meng H 2003 Digital holography of particle fields: reconstruction by use of complex amplitude. *Applied Optics* **42**, 827–833.

Pavani SRP, Thompson MA, Biteen JS, Lord SJ, Liu N, Twieg RJ, *et al*. 2009 Three-dimensional, single-molecule fluorescence imaging beyond the diffraction limit by using a double-helix point spread function. *Proceedings of the National Academy of Sciences* **106**(9), 2995–2999.

Pellat-Finet P 1994 Fresnel diffraction and the fractional-order Fourier transform. *Optics Letters* **19**(18), 1388–1390.

Poon TC, Yatagai T and Juptner W 2006 Digital holography–coherent optics of the 21st century: introduction. *Applied Optics* **45**(5), 821.

Repetto L, Piano E and Pontiggia C 2004 Lensless digital holographic microscope with light-emitting diode illumination. *Optics Letters* **29**(10), 1132–1134.

Rivenson Y, Stern A and Javidi B 2010 Compressive Fresnel holography. *Display Technology, Journal of* **6**(10), 506–509.

Royer H 1974 An application of high-speed microholography: the metrology of fogs. *Nouv. Rev. Opt* **5**, 87–93.

Seifi M, Denis L and Fournier C 2013a Fast and accurate 3D object recognition directly from digital holograms. *JOSA A* **30**(11), 2216–2224.

Seifi M, Fournier C, Denis L, Chareyron D and Marie JL 2012 Three-dimensional reconstruction of particle holograms: a fast and accurate multiscale approach. *JOSA A* **29**(9), 1808–1817.

Seifi M, Fournier C, Grosjean N, Meess L, Marié JL and Denis L 2013b Accurate 3D tracking and size measurementof evaporating droplets using an in-line digital holography and inverse problems reconstruction approach. *Optics Express* **21**(23), 27964–27980.

Shimobaba T, Ito T, Masuda N, Abe Y, Ichihashi Y, Nakayama H, *et al*. 2008 Numerical calculation library for diffraction integrals using the graphic processing unit: the GPU-based wave optics library. *J. Opt. A: Pure Appl. Opt* **10**(075308), 075308.

Sotthivirat S and Fessler JA 2004 Penalized likelihood image reconstruction for digital holography. *Journal of the Optical Society of America A* **21**(5), 737–750.

Soulez F, Denis L, Fournier C, Thiébaut E and Goepfert C 2007a Inverse problem approach for particle digital holography: accurate location based on local optimisation. *Journal of the Optical Society of America A* **24**(4), 1164–1171.

Soulez F, Denis L, Thiébaut E, Fournier C and Goepfert C 2007b Inverse problem approach in particle digital holography: out-of-field particle detection made possible. *Journal of the Optical Society of America A* **24**(12), 3708–3716.

Stern A and Javidi B 2006 Improved-resolution digital holography using the generalized sampling theorem for locally band-limited fields. *Journal of the Optical Society of America A* **23**(5), 1227–1235.

Tyler G and Thompson B 1976 Fraunhofer holography applied to particle size analysis a reassessment. *Journal of Modern Optics* **23**(9), 685–700.

Verpillat F, Joud F, Desbiolles P and Gross M 2011 Dark-field digital holographic microscopy for 3D-tracking of gold nanoparticles. *Optics Express* **19**(27), 26044–26055.

Virant M and Dracos T 1997 3D PTV and its application on Lagrangian motion. *Measurement Science and Technology* **8**(12), 1539.

Volk R, Mordant N, Verhille G and Pinton JF 2008 Laser doppler measurement of inertial particle and bubble accelerations in turbulence. *EPL (Europhysics Letters)* **81**(3), 34002.